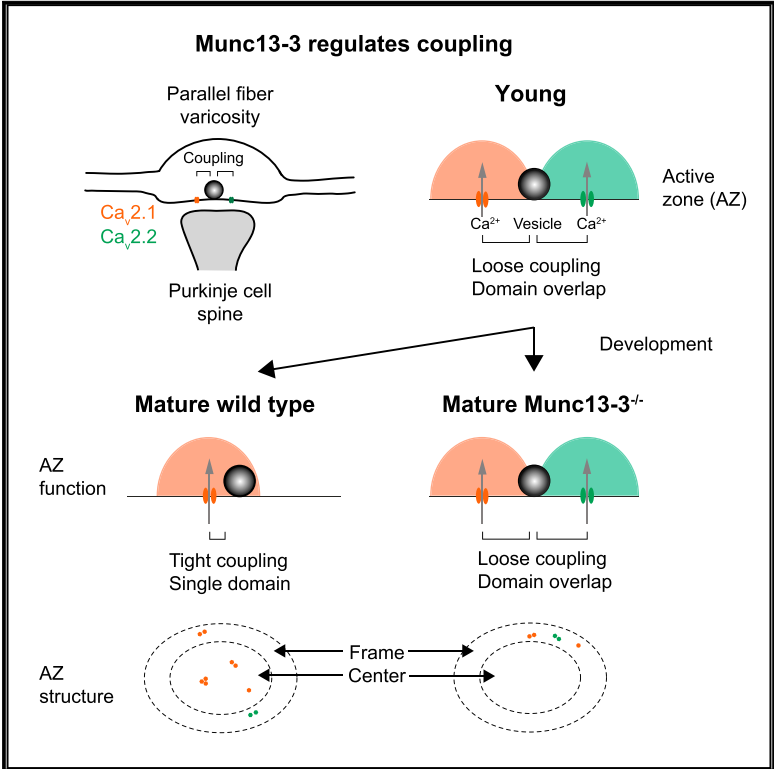


Munc13-3 Is Required for the Developmental Localization of Ca²⁺ Channels to Active Zones and the Nanopositioning of Ca_v2.1 Near Release Sensors

Graphical Abstract



Authors

Valentin Kusch, Grit Bornschein, Desiree Loreth, ..., Manfred Heckmann, Jens Eilers, Hartmut Schmidt

Correspondence

hartmut.schmidt@medizin.uni-leipzig.de

In Brief

Central synapses shift from microdomain to nanodomain coupling between Ca²⁺ channels and release sensors during development. Kusch et al. show that Munc13-3 is a critical regulator of this process. Munc13-3 differentially regulates density and localization of Ca_v2.1 and Ca_v2.2 channels and establishes nanodomain coupling between Ca_v2.1 channels and release sensors.

Highlights

- Munc13-3 mediates nanodomain coupling during postnatal synapse maturation
- Nanodomain coupling is established between Ca_v2.1 channels and release sensors
- Ca_v2.1 and Ca_v2.2 domain-overlap topography shifts to Ca_v2.1 single-domain topography
- Munc13-3 differentially regulates density and localization of Ca_v2.1 and Ca_v2.2



Munc13-3 Is Required for the Developmental Localization of Ca²⁺ Channels to Active Zones and the Nanopositioning of Ca_v2.1 Near Release Sensors

Valentin Kusch,^{1,6} Grit Bornschein,^{1,6} Desiree Loreth,² Julia Bank,² Johannes Jordan,² David Baur,¹ Masahiko Watanabe,³ Akos Kulik,^{2,4} Manfred Heckmann,⁵ Jens Eilers,¹ and Hartmut Schmidt^{1,7,*}

¹Carl-Ludwig-Institute for Physiology, Medical Faculty, University of Leipzig, Liebigstrasse 27, 04103 Leipzig, Germany

²Institute of Physiology II, Faculty of Medicine, University of Freiburg, 79104 Freiburg, Germany

³Department of Anatomy, Graduate School of Medicine, Hokkaido University, Sapporo 060-8638, Japan

⁴BIOSS Centre for Biological Signalling Studies, University of Freiburg, 79104 Freiburg, Germany

⁵Department of Physiology, Neurophysiology, Medical Faculty, University of Würzburg, Röntgenring 9, 97070 Würzburg, Germany

⁶These authors contributed equally

⁷Lead Contact

*Correspondence: hartmut.schmidt@medizin.uni-leipzig.de

<https://doi.org/10.1016/j.celrep.2018.02.010>

SUMMARY

Spatial relationships between Ca_v channels and release sensors at active zones (AZs) are a major determinant of synaptic fidelity. They are regulated developmentally, but the underlying molecular mechanisms are largely unclear. Here, we show that Munc13-3 regulates the density of Ca_v2.1 and Ca_v2.2 channels, alters the localization of Ca_v2.1, and is required for the development of tight, nanodomain coupling at parallel-fiber AZs. We combined EGTA application and Ca²⁺-channel pharmacology in electrophysiological and two-photon Ca²⁺ imaging experiments with quantitative freeze-fracture immunoelectron microscopy and mathematical modeling. We found that a normally occurring developmental shift from release being dominated by Ca²⁺ influx through Ca_v2.1 and Ca_v2.2 channels with domain overlap and loose coupling (microdomains) to a nanodomain Ca_v2.1 to sensor coupling is impaired in Munc13-3-deficient synapses. Thus, at AZs lacking Munc13-3, release remained triggered by Ca_v2.1 and Ca_v2.2 microdomains, suggesting a critical role of Munc13-3 in the formation of release sites with calcium channel nanodomains.

INTRODUCTION

The details of the nanoscopic arrangement between voltage-activated Ca²⁺ channels (Ca_vs) and the sensors for transmitter release are crucial for setting fundamental synaptic properties, including release probability (p_r) and plasticity (Eggermann et al., 2011). Synapses with different transmission characteristics were described to operate at different Ca_v-to-sensor coupling configurations ranging from loose (microdomain) (Vyleta and Jonas, 2014) to tight (nanodomain) coupling (Bucurciuciu et al., 2008; Schmidt et al., 2013). At the calyx of Held (Fed-

chyshyn and Wang, 2005) and the parallel fiber (PF)-to-Purkinje neuron (PN) synapse (Baur et al., 2015), the coupling distance undergoes substantial developmental tightening, associated with changes in p_r and short-term plasticity.

The cellular and molecular mechanisms regulating active zone (AZ) topography and mediating tight coupling during development remain poorly understood. Several proteins, including RIM, RIM-BP, and ELKS, have known functions in synaptic vesicle docking and recruitment of Ca_vs (Südhof, 2012). In addition, Septin5 has been suggested to operate as a developmentally downregulated “spacer” between Ca_vs and release sensors at the calyx of Held; that is, its downregulation is permissive to the establishment of tight coupling (Yang et al., 2010). However, no developmental mediators of tight coupling were identified to date (Eggermann et al., 2011).

Munc13-3 is strongly expressed in PF varicosities (PF_vs). Notably, its expression is upregulated during development (Augustin et al., 1999), and Munc13-3-deficient synapses have decreased p_r (Augustin et al., 2001; Ishiyama et al., 2014). These findings would be consistent with a role of Munc13-3 in regulating AZ topography and coupling distances during development. To test this, we investigated PF-PN synapses of Munc13-3 mutants in a postnatal developmental context. Our data suggest that Munc13-3 is a critical organizer of release sites. It differentially regulates density and localization of Ca_v2.1 (P/Q-type) and Ca_v2.2 (N-type) channels at the AZ and acts as a developmental mediator of nanodomain coupling between release sensors and Ca_v2.1 channels.

RESULTS

Impaired Developmental Tightening of Coupling in Munc13-3^{-/-}

To quantify the coupling distance at wild-type (WT; Munc13-3^{+/+}) littermates and C57Bl6 WT) and Munc13-3^{-/-} (knockout [KO]) AZs of PF_vs, we first analyzed the effects of the Ca²⁺ chelator EGTA on release (Figure 1). A major differentiating feature distinguishing loose from tight coupling is that this kinetically slow Ca²⁺ chelator is much more effective in reducing release in loose



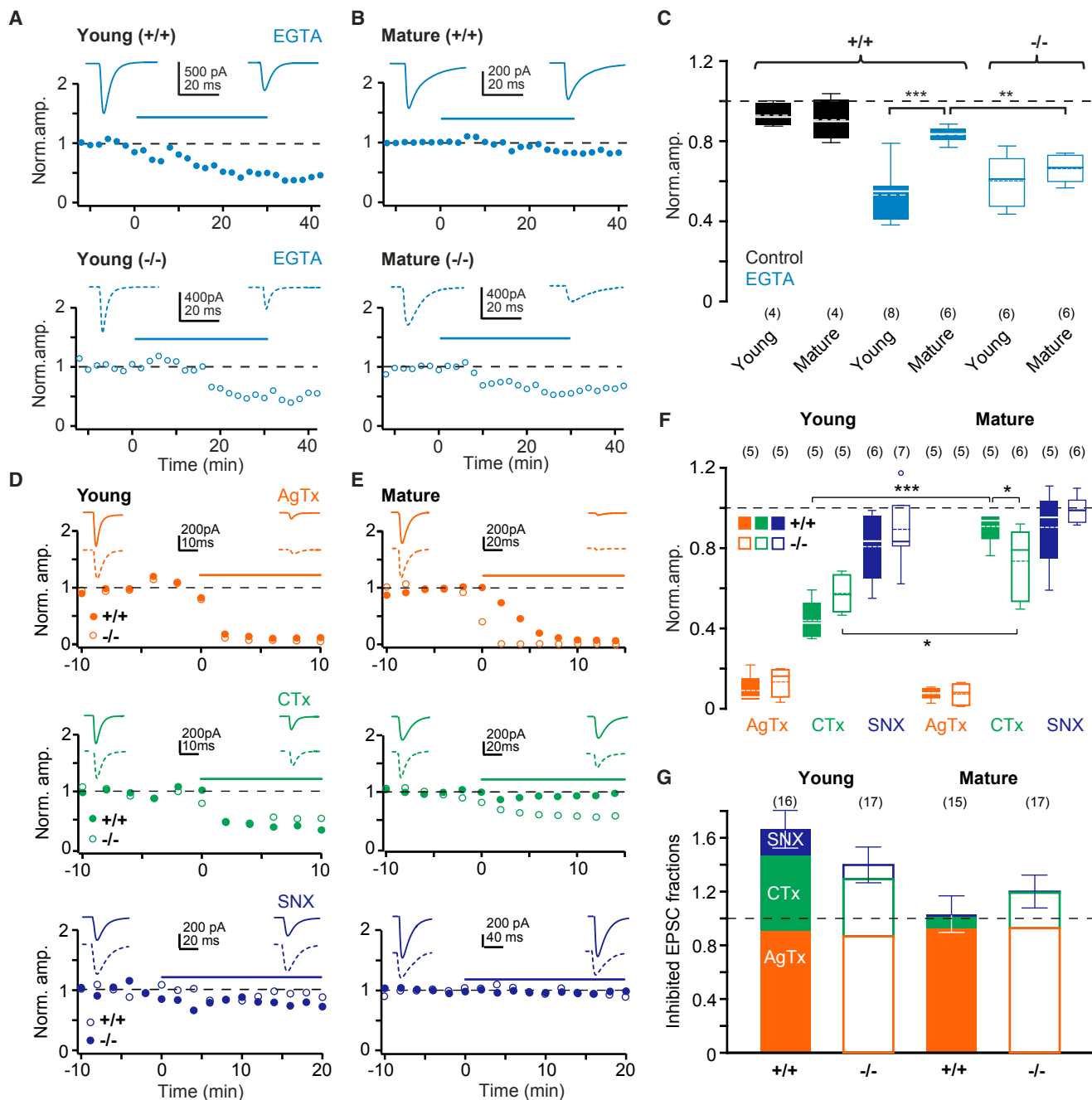


Figure 1. Munc13-3^{-/-} Regulates Coupling Topography during Development

(A) Top: example of EGTA-AM effects on baseline normalized EPSC amplitudes at young Munc13-3^{+/+} (+/+) synapses. EGTA-AM was applied for 30 min (blue bar) and rinsed for 10 min (test period). Insets: averaged EPSCs during baseline and test period (stimulus artifacts removed). Bottom: the same for Munc13-3^{-/-} (-/-).

(B) As in (A), but for mature mice.

(C) Summary of EGTA effects (blue) on normalized EPSC amplitudes (control, DMSO/Pluronic, black; Figure S1). Solid lines, medians; dashed lines, means; boxes, IQRs; whiskers, farthest points within 1.5-fold IQR; n in brackets.

(D) Examples of ω -agatoxin-IVA (AgTx; 250 nM), ω -conotoxin GVIA (CTx; 5 μ M) and SNX-482 (SNX; 500 nM) effects on EPSC amplitudes in young WT (+/+, filled circles) and KO (-/-, empty circles). Effects were quantified from >5 min intervals after establishment of stable block (test period). Insets: averaged EPSCs during baseline and test period in WT (+/+; straight lines) and KO (-/-; dashed lines).

(E) As in (D), but for mature mice.

(F) Summary of toxin effects.

(G) Sums of AgTx-, CTx-, and SNX-sensitive EPSC fractions.

than in tight coupling regimes (Adler et al., 1991). Previously, we found that loading of PF_v with membrane-permeable EGTA (EGTA-AM) significantly affects release from young (postnatal day [P] 8–10) but not from matured (P21–P24) PF terminals onto PN in the WT (Baur et al., 2015) and that EGTA-AM affects release at mature PF to basket cell (BC) synapses in Munc13-3^{-/-} but not in WT mice (Ishiyama et al., 2014). These data would be compatible with a critical role of Munc13-3 in the maturation of the release process. If true, one would expect that both release at young and matured mutant PF-to-PN synapses would be affected significantly by EGTA, whereas in the WT, strong EGTA effects would be expected only at young synapses but not at mature ones. To test this, we analyzed excitatory post-synaptic currents (EPSCs) at differentially aged synapses before, during, and after their incubation with 10 μM EGTA-AM. Although rather ill defined, an EGTA concentration < 10 mM can be expected under our experimental conditions in both young and mature PF synapses (Baur et al., 2015), a concentration that affects release only if coupling is loose but not if it is tight (Vyleta and Jonas, 2014).

In Munc13-3^{+/+}, EPSC amplitudes of young connections were affected significantly by EGTA compared with control (median reductions of 45%, interquartile range [IQR] 42%–59%, n = 8 cells, and 8%, IQR 3%–12%, n = 4 cells, respectively, p < 0.001), whereas at mature connections, EGTA was ineffective (median reduction of 16% [IQR 15%–18%, n = 6 cells] versus 10% [IQR 2%–16%, n = 4 cells] in control, p = 0.251; Figures 1A–1C and S1A). In young mutants, EGTA was similarly effective in intercepting release as in Munc13-3^{+/+} (median reduction of 39% [IQR 31%–51%, n = 6], p = 0.221). Remarkably, EGTA remained highly effective also at mature KO terminals, not different from its effectiveness in young animals (33% [IQR 27%–39%, n = 6], p = 0.324).

This finding of similar EGTA effects at young and mature mutant synapses is consistent with the hypothesis that Munc13-3 plays a role in the development of tight coupling. It argues against the alternative hypothesis that Munc13-3 mainly functions in increasing the Ca²⁺ sensitivity of the release process (see discussion in Ishiyama et al., 2014). If the latter were true, one would have to assume the unlikely scenario that the loss of sensor sensitivity increase in the absence of Munc13-3 is counterbalanced precisely by the developmental tightening of coupling such that release from young and mature mutant terminals is affected almost identically by EGTA. Because this is still conceivable, we used simplified computer simulations of Ca²⁺ dynamics and transmitter release to test whether the latter scenario could be possible theoretically (Figure S1B). The charge of the simulated Ca²⁺ influx was adjusted such that the simulations yielded p_r of 0.25 and 0.025 at coupling distances of 25 and 60 nm, respectively, mimicking mature and immature PF AZs (Baur et al., 2015; Foster et al., 2005). In the simulation, 1.5 mM EGTA reduced release by 35% in the loose coupling scenario and was almost ineffective if coupling was tight. We then reduced k_{on} of the release sensor (i.e., reduced its Ca²⁺ sensitivity) in the tight coupling simulation such that p_r was reduced to 0.025. Interestingly, under these conditions EGTA remained ineffective in interfering with release. Thus, at least in the simulations, differential effects of low concentrations of EGTA indicate

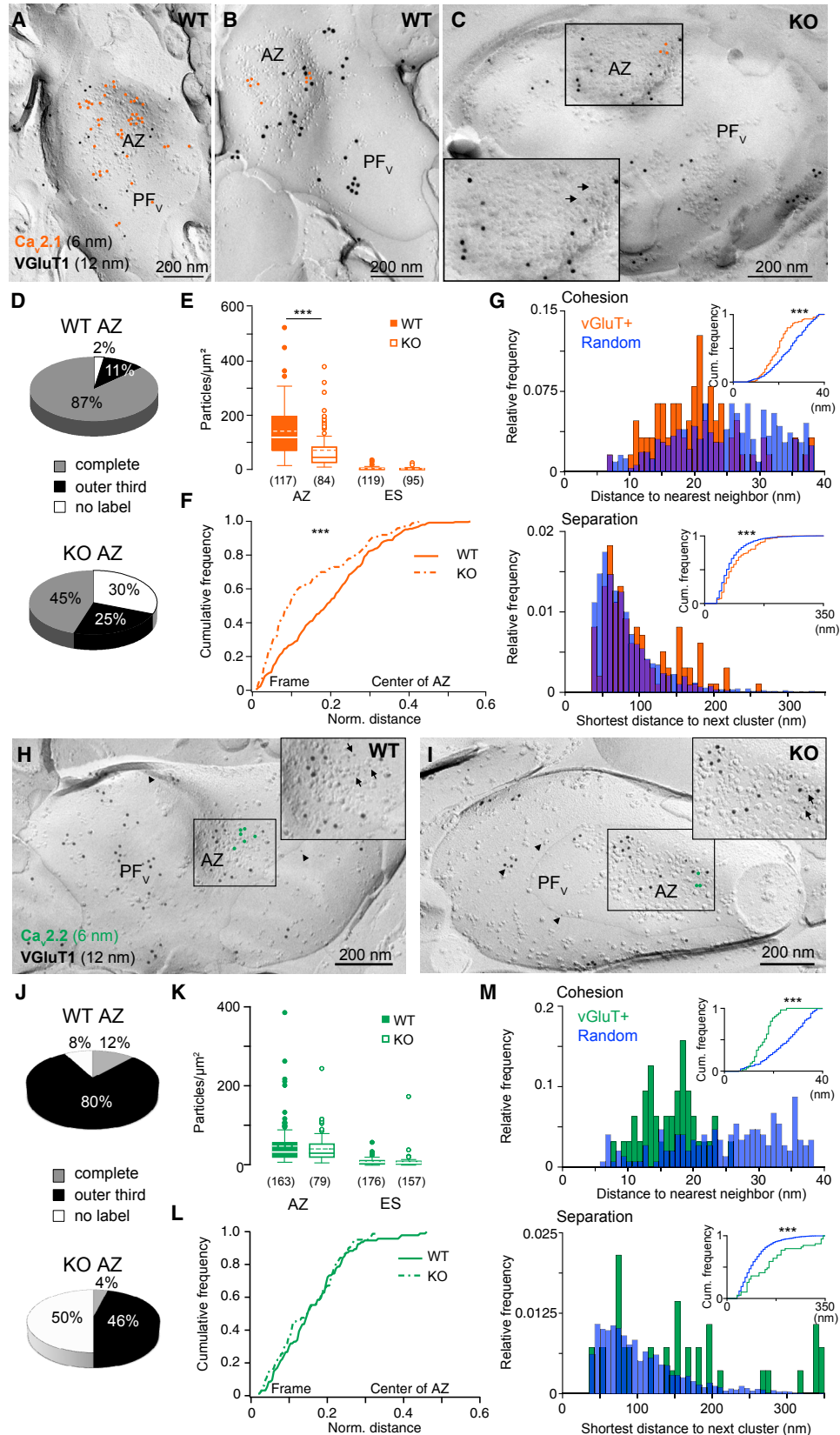
differences in coupling distance rather than in the Ca²⁺ sensitivity of release, suggesting impaired tightening of coupling in Munc13-3^{-/-}.

Impaired Developmental Switch from Domain-Overlap to Single-Domain Topography in Munc13-3^{-/-}

We proceeded by analyzing the spatial relationships between Ca_vs and release sensors and the Ca_v subtypes involved in driving release. At young WT PF terminals, fusion of a vesicle is controlled via Ca²⁺ influx through several channels (domain-overlap topography [DOT]; Baur et al., 2015; Mintz et al., 1995), while at mature terminals a vesicle is controlled by a single channel or dense cluster of few Ca_vs (single-domain topography [SDT]; Baur et al., 2015; Schmidt et al., 2013). Differential effects of sub-saturating concentrations of the Ca_v blocker Cd²⁺ on paired-pulse ratios (PPRs) provide a means to distinguish between the two topographies. Because of its slow unbinding, Cd²⁺ increases the PPR in case of a DOT, whereas it remains constant for an SDT (Scimemi and Diamond, 2012).

We quantified PPR in the presence of Cd²⁺ and normalized it to PPR under control conditions (PPR_{Cd}/PPR_{ctrl}; Figures S1C–S1E). PPR significantly increased in the presence of Cd²⁺ in young WT (PPR_{Cd}/PPR_{ctrl} = 1.13 [0.98–1.57], n = 14, p < 0.001 versus an identical distribution around 1), which is consistent with a DOT at immature AZs. At mature WT connections, on the other hand, the PPR ratio was unity (PPR_{Cd}/PPR_{ctrl} = 1.0 [0.92–1.09], n = 12, p = 0.319 versus 1), consistent with an SDT. Recordings from young KO connections revealed PPR_{Cd}/PPR_{ctrl} of 1.24 (1.07–1.45, n = 8, p < 0.001 versus 1), a value not different from the young WT (p = 0.474). Remarkably, the PPR ratio at mature mutant connections was elevated significantly above the mature WT unity ratio (PPR_{Cd}/PPR_{ctrl} = 1.15 [1.02–1.23], n = 8, p = 0.043, p < 0.001 versus 1), indicating that in Munc13-3^{-/-}, the developmental switch from DOT to SDT is impaired.

We next analyzed the effects of Ca_v subtype specific toxins, using the Ca_v2.1 blocker ω-agatoxin-IVA (AgTx; 250 nM) and the Ca_v2.2 blocker ω-conotoxin GVIA (CTx; 5 μM) at concentrations known to completely block Ca²⁺ influx at PF-PN synapses (Mintz et al., 1995). Ca_v2.3 (R-type) were inhibited by SNX-482 (SNX; 500 nM), a toxin producing specific but incomplete block (Myoga and Regehr, 2011). Importantly, use of these toxins gives insights into not only the Ca_v subtypes driving release but also the AZ topography. For an SDT in which a given vesicle is linked to either of the Ca_vs, the sum of the toxin-sensitive release fractions will not exceed release measured in the absence of toxins (“linear” summation). Contrariwise, for an AZ at which release of a vesicle is controlled by overlapping Ca²⁺ domains of different Ca_v subtypes (DOT), the sum of the blocked release fractions can exceed the control value because of the non-linear dependency of release on Ca²⁺ (“supralinear” summation; Mintz et al., 1995). We found that irrespective of genotype and age AgTx blocked release almost completely (young WT 94% [88%–95%, n = 5]; young KO 84% [81%–93%, n = 5]; mature WT 92% [90%–93%, n = 5]; mature KO 92% [88%–98%, n = 5]; p = 0.477 [genotype], p = 0.175 [age]), while CTx (block of 6% [5%–11%, n = 5] and SNX (4% [0%–17%, n = 5] were almost ineffective in mature WT. Hence, in mature WT the



(legend on next page)

fractional block by the toxins added up to $103 \pm 13\%$ ($n = 15$, $p = 0.873$ versus 100%), consistent with SDT (Figures 1D–1G). At young synapses of WT (CTx: block of 57% [51%–64%], $n = 5$; SNX: 16% [5%–31%], $n = 6$) and KO (CTx: 43% [34%–51%], $n = 5$; SNX: 17% [0%–17%], $n = 7$), CTx in particular produced a significantly stronger block than in mature WT ($p < 0.001$), such that the sum of the blocked release fractions substantially exceeded 100% (WT: $166 \pm 14\%$, $n = 16$, $p = 0.002$; KO: $140 \pm 13\%$, $n = 17$, $p = 0.042$). This is consistent with a DOT at young synapses of both genotypes. Remarkably, also at mature mutant synapses, the CTx effect was significantly larger than in mature WT (21% [13%–45%], $n = 6$, $p = 0.030$), while the SNX block was similarly small as in mature WT (1% [–2% to 6%], $n = 6$, $p = 0.2$). As a result, the sum of the toxin-sensitive release fractions exceeded 100% ($120 \pm 12\%$, $n = 17$) also in mature mutant synapses. Thus, DOT-indicating supra-linear summation occurred irrespective of the genotype at immature synapses but also at mature KO synapses, suggesting an impaired developmental switch from DOT to SDT in the KO.

Subcellular Organization of Ca_v Is Regulated by Munc13-3

We investigated the surface density and distribution of $Ca_v2.1$ and $Ca_v2.2$ at mature PF_vs by quantitative SDS-digested freeze-fracture replica immunoelectron microscopy (SDS-FRL EM; Figure 2). Our antibodies were raised against intracellular epitopes of the target proteins, resulting in labeling on the protoplasmic face (P-face) of the replicas (Althof et al., 2015; Holderith et al., 2012). PF_vs were identified by their characteristic oval shape and positive immunostaining for the vesicular glutamate transporter 1 (vGluT1), which distinguishes PF_vs from climbing-fiber terminals in matured cerebellum (Miyazaki et al., 2003). Although vGluTs are vesicular proteins, they are typically detected also on the synaptic and extrasynaptic plasma membrane of varicosities (Indriati et al., 2013). AZs were identified by their high density of intramembrane particles and their concave shape. AZ areas in WT (median 0.068 [IQR 0.046 – 0.093] μm^2 , $n = 297$) were larger than in the KO (median 0.056 [IQR 0.039 – 0.077] μm^2 , $n = 277$) ($p < 0.001$).

Immunoparticles for $Ca_v2.1$ were detected in virtually all PF_vs in WT (98% [$n = 120$]), but in only 70% of PF_vs in the KO ($n = 120$). In addition, they appeared to be differentially distributed over the

AZs between the two genotypes (Figure 2D). We semiquantitatively assessed the latter observation by subdividing the AZ into an outer third (termed “frame” here) and the remaining inner part (“center”; Figure S2A). In WT, particles were distributed over the complete AZ of the vast majority (87%) of PF_vs. Their density, as calculated from immunopositive PF_vs, was high over the AZ (118 [72–196] particles/ μm^2 , average of ~ 8 particles/AZ) and very low at the extrasynaptic membrane (ES; 0 [0–4] particles/ μm^2). The smaller number of $Ca_v2.1$ particles per AZ we found in mice compared with AZs of older rats (Indriati et al., 2013) may result from differences in species, age, or size of AZs.

In contrast to WT, at mutant AZs, $Ca_v2.1$ labeling was frequently restricted to the frame (25%), and the density was significantly lower (45 [26–80] particles/ μm^2 , average 2–3 particles/AZ, $p < 0.001$) than in WT, whereas the density at the ES remained unchanged (0.9 [0–3] particles/ μm^2 , average ~ 1 particle/ES, $p = 0.71$; Figure 2E). These findings indicate a function of Munc13-3 in determining the subcellular location and density of $Ca_v2.1$. To quantify this, we measured the shortest distances between particles and the rim of AZs (Figures 2F and S2B). The resulting distance distributions were significantly different between genotypes ($p < 0.001$), with a shift toward smaller distances in the KO. This agrees with the observed frequent restriction of $Ca_v2.1$ to the frame of AZs in the KO. Furthermore, we found that in WT $Ca_v2.1$ were organized in clusters compared with random distributions of particle cohesion ($p < 0.0001$) and cluster separation ($p < 0.001$), respectively (Figure 2G; cf. Althof et al., 2015; Holderith et al., 2012; Indriati et al., 2013). For the KO, the low particle density impeded similar analysis.

In contrast to $Ca_v2.1$, $Ca_v2.2$ localized mainly to the frame of AZs in WT and KO (Figures 2H and 2I), $Ca_v2.2$ showed stronger immunoreactivity along the ES (WT: 6 [2–10] particles/ μm^2 ; KO: 4 [2–8] particles/ μm^2 ; $p = 0.13$), and a higher proportion of PF_vs showed no labeling for the protein in both genotypes (WT: 8%, $n = 157$; KO: 50%, $n = 177$; Figure 2J). Notably, when considering only AZs containing $Ca_v2.2$, neither the average particle densities between WT (32 [19–56] particles/ μm^2 , on average ~ 2 particles/AZ) and KO (29 [19–51] particles/ μm^2 , on average ~ 2 particles/AZ, $p = 0.42$; Figure 2K) nor their distance distributions (Figure 2L; $p = 0.36$) were different. Like $Ca_v2.1$, $Ca_v2.2$ were also organized in clusters in WT ($p < 0.0001$ for cohesion and

Figure 2. Munc13-3 Regulates Density and Distribution of $Ca_v2.1$

(A and B) SDS-FRL replica images showing strong (A) and moderate (B) labeling for $Ca_v2.1$ (6 nm particles, highlighted in orange) in WT distributed over the entire AZ (A) or restricted to its outer third (B) of vGluT1-positive (12 nm) PF_vs.

(C) As in (A) and (B), but for Munc13-3^{-/-}. Note the restriction of $Ca_v2.1$ particles to the frame of the AZ. Inset: particles (arrows) without coloring.

(D) Fractions of AZs in WT and KO with labeling for $Ca_v2.1$ being absent (white), distributed over the entire AZ (gray), or restricted to its outer third (black; cf. Figure S2).

(E) Median and IQR surface densities of $Ca_v2.1$ in immuno-positive PF_vs for AZ and ES in WT and KO. Solid lines, medians; dashed lines, means; boxes, IQRs; whiskers, farthest points within 1.5fold IQR; points, outlier; n in brackets.

(F) Cumulative distributions of normalized particle distances to the rim ($x = 0$) of the AZ in WT (solid line) and KO (dashed line) on the basis of 30 randomly selected immunopositive AZs per genotype.

(G) Distributions of distances between nearest particles (cohesion) and shortest distances between clusters (separation) for AZs of vGluT1+ PF_vs (orange) compared with random distributions (blue). Insets show the corresponding cumulative probabilities. Note the significant difference between real and random distributions, indicating $Ca_v2.1$ clustering.

(H–M) As in (A)–(G), but for $Ca_v2.2$ (6 nm, highlighted in green, arrows in insets). Electron micrograph showing $Ca_v2.2$ labeling in WT (H) and KO (I), AZ fractions (J), particle densities (K), cumulative distributions of normalized particle distances (L), and particle cohesion (upper) and cluster separation (lower) (M). Note that particles localized mainly to the frame of AZs and occasionally also to the ES (arrowheads) of vGluT1-positive (12 nm) PF_vs in both genotypes.

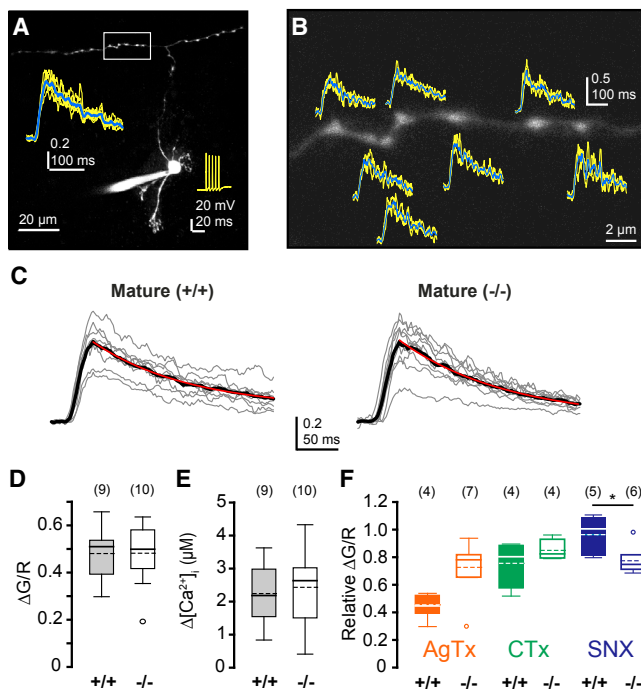


Figure 3. Ca^{2+} Transients Are Not Different between WT and KO but Depend on Different Ca_v Subtypes

(A) Two-photon image of a mature granule cell loaded via a patch pipette containing 200 μM Fluo-5F and 100 μM Alexa 594. Insets: average $\Delta\text{G/R}$ (yellow) from the boutons in B (white box, grand average in blue) during burst stimulation (5 APs, 200 Hz).

(B) PF boutons from which fluorescence changes were recorded in line scans. Insets: $\Delta\text{G/R}$ from each bouton (three individual recordings in yellow, average in blue).

(C) Averaged $\Delta\text{G/R}$ signals from boutons of WT (+/+, left) and KO (-/-, right). Averages of recordings from individual cells in gray, grand averages in black, exponential fits to the decay in red.

(D and E) Comparison of $\Delta\text{G/R}$ (D) and corresponding $[\text{Ca}^{2+}]_i$ (E) between WT (gray) and KO (white). Box (IQR) and whisker (last points within 1.5-fold IQR) plots with outlier (points), medians (solid lines), and means (dashed lines); n in brackets.

(F) Effects of ω -agatoxin-IVA (AgTx; 250 nM), ω -conotoxin GVIA (CTx; 5 μM) and SNX-482 (SNX; 500 nM) normalized to control.

separation; Figure 2M). Thus, in the KO $\text{Ca}_v2.1$ particles were frequently restricted to the outer third of AZs, where $\text{Ca}_v2.2$ also mainly localized, a result consistent with $\text{Ca}_v2.1$ and $\text{Ca}_v2.2$ signaling domain overlap in the mature KO.

Presynaptic Ca^{2+} Influx

To investigate if Ca^{2+} influx is affected in $\text{Munc13-3}^{-/-}$, we performed two-photon Ca^{2+} imaging at mature terminals using the Ca^{2+} indicator dye Fluo-5F (200 μM , $K_d = 1.44$ mM) and the Ca^{2+} -insensitive dye Alexa 594 (100 μM). To facilitate pharmacological dissection, Ca^{2+} signals ($\Delta\text{G/R}$; Sabatini et al., 2002) were induced by brief bursts of 5 action potentials (APs) at 200 Hz (Figures 3A and 3B). Signals in WT had an amplitude of 0.51 (0.44–0.53, $n = 9$) $\Delta\text{G/R}$ and decayed with a time constant (τ) of 108 (90–125) ms. The estimated change in the intracellular free Ca^{2+} concentration ($[\text{Ca}^{2+}]_i$) was 2.2 [1.7–3.0] μM

(Figures 3C–3E). Interestingly, Ca^{2+} signals in mutant boutons were not different from the WT (0.50 [0.44–0.56] $\Delta\text{G/R}$, $n = 10$, $p = 0.967$; $\tau = 122$ [110–128] ms, $p = 0.348$; 2.6 [1.5–3.0] μM $[\text{Ca}^{2+}]_i$, $p = 0.713$). To assure that dye saturation did not affect our analysis, we performed additional experiments using the low-affinity Ca^{2+} indicator Oregon green 488 BAPTA-5N (OG-5N; 300 μM ; $K_d = 24$ μM ; Delvendahl et al., 2015) in conjunction with Alexa 594 (Figures S3A and S3B). Again no significant difference in Ca^{2+} signals between the two genotypes was detected (WT: 0.38 [0.28–0.47] $\Delta\text{G/R}$, $n = 6$; KO: 0.56 [0.31–0.62] $\Delta\text{G/R}$, $n = 8$, $p = 0.573$). This is consistent with previous work (Ishiyama et al., 2014) but not readily understood in light of our EM results. We therefore analyzed effects of Ca_v subtype specific blockers on the Ca^{2+} signals.

In WT, block of $\text{Ca}_v2.1$ by AgTx and $\text{Ca}_v2.2$ by CTx reduced Ca^{2+} signals by 55% (49%–60%, $n = 4$) and 20% (12%–27%, $n = 4$), respectively, while inhibition of $\text{Ca}_v2.3$ by SNX had almost no impact (0% [–9% to 18%], $n = 5$; Figure 3F). These values agree with those previously reported for PF terminals of young rats (Mintz et al., 1995; Myoga and Regehr, 2011). In the KO, AgTx was less effective in most cells (on average 22% [19%–32%], $n = 7$, $p = 0.073$), which is consistent with the average reduced density of $\text{Ca}_v2.1$ at mutant AZs. In one of seven cells, similar effects as in the WT were observed, which likely reflects that part of the mutant PF_vs lacked $\text{Ca}_v2.2$, which will result in an increased relative contribution of $\text{Ca}_v2.1$ -mediated influx to the global Ca^{2+} signal. CTx was as effective in the KO (18% [10%–20%] block, $n = 4$) as in the WT ($p = 0.686$), while SNX had a stronger effect than in WT (25% [24%–28%], $n = 6$, $p = 0.017$). Together these data indicate that in WT and KO, comparable numbers of $\text{Ca}_v2.2$ channels open during an AP, while the average number of open $\text{Ca}_v2.1$ or $\text{Ca}_v2.3$ channels are reduced or increased, respectively, in the KO.

AZ Models in the Presence and Absence of Munc13-3

To derive quantitative estimates about the role of Munc13-3 in organizing the AZ, we constructed kinetic three-dimensional (3D) reaction diffusion models of Ca^{2+} dynamics and transmitter release. Models were empirically constrained by the present and previously published experimental data (Table S1) and adjusted to the Ca^{2+} imaging data (Figures S3C–S3F).

The simulations included a presynaptic AP waveform, voltage-dependent gating, and conductance schemes for $\text{Ca}_v2.1$, $\text{Ca}_v2.2$, and $\text{Ca}_v2.3$ channels (Li et al., 2007) as well as ATP and calretinin (CR; 20% immobile fraction; mobile CR corrected for whole-cell washout; Faas et al., 2007) as endogenous Ca^{2+} buffers and Fluo-5F as exogenous buffer. The contribution of open Ca_v subtypes to total Ca^{2+} influx was estimated according to the fractional susceptibility of the measured Ca^{2+} signals to the subtype specific blockers. The simulations reproduced the WT Ca^{2+} signals if six $\text{Ca}_v2.1$, five or six $\text{Ca}_v2.2$, and two $\text{Ca}_v2.3$ opened in a PF_v during the AP. Considering that the open probabilities are ~0.7–0.9, respectively (Li et al., 2007), these estimates are in good agreement with the particle counts (AZ and ES) from the SDS-FRL, which can be taken as indicative of high labeling efficacy for $\text{Ca}_v2.1$ and $\text{Ca}_v2.2$ in SDS-FRL at PF_v, in agreement with a previous report (Indriati et al., 2013). Ca^{2+} signals of mutant terminals were modeled with four

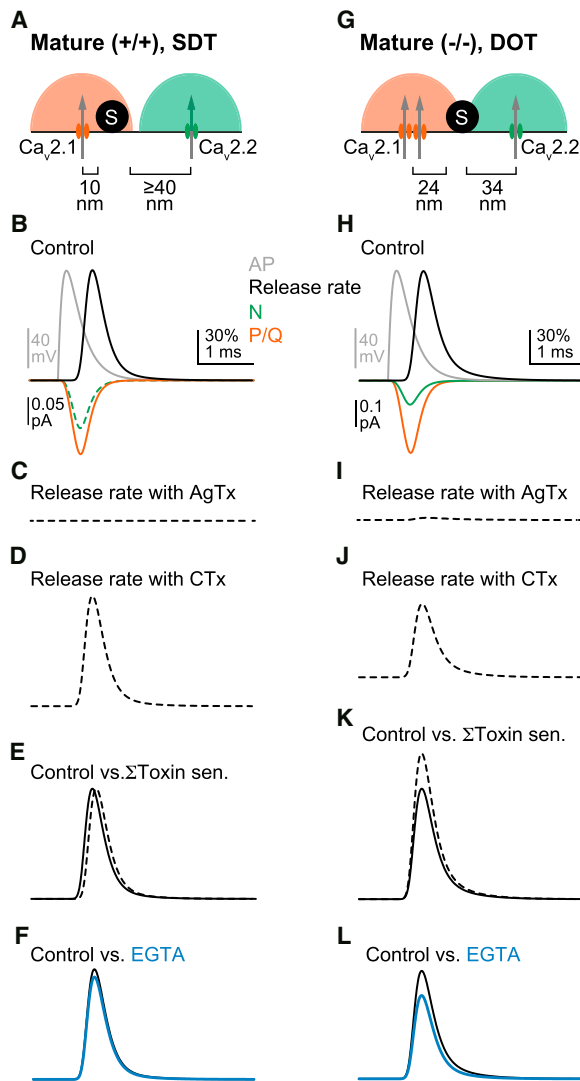


Figure 4. Simulations Indicate Perturbed Tightening of Coupling in *Munc13-3*^{-/-}

(A) Model (cf. Table S1) of mature WT AZs. Ca_v2.1 (orange) and Ca_v2.2 (green) had coupling distances of 10 and ≥ 40 nm, respectively, to release sensors (S).
 (B) AP (gray), Ca²⁺ current through one open Ca_v2.1 (orange) and one open Ca_v2.2 (dashed green), and the self-normalized release rate (black; $p_r = 0.25$). Dashing of the green line indicates that Ca_v2.2 contributed < 0.1% to release.
 (C) Release rate (dashed black line) if influx occurred only through Ca_v2.2, representing block of Ca_v2.1 by AgTx.
 (D) As in (C), but for block of Ca_v2.2 by CTx.
 (E) Sum of toxin-sensitive release rate fractions (dashed line) compared with the control release rate from (B) (solid line); shown with temporal offset (100 μs) to control for clarity.
 (F) Release rates under control conditions (black) and in the presence of 4.5 mM EGTA (blue; $p_r = 0.23$).
 (G–L) As in (A)–(F), but for the mature KO.
 (G) Ca²⁺ influx occurred through two open Ca_v2.1 (orange) and one Ca_v2.2 (green) channel with the indicated distances to S.
 (H) As in (B) ($p_r = 0.124$). Ca²⁺ current through Ca_v2.2 is shown here as solid green line because of its larger contribution to release.
 (I) As in (C). Simulated block of Ca_v2.1 resulted in 97% reduction of p_r .
 (J) As in (D). Simulated block of Ca_v2.2 reduced p_r by 32%.

Ca_v2.1, five Ca_v2.2, and three Ca_v2.3 channels opening during an AP, consistent with altered AgTx and SNX sensitivity and reduced Ca_v2.1 density.

For modeling transmitter release, Fluo-5F and washout correction for CR were removed from the simulations, and the “allosteric” sensor scheme was included (Figure 4; Lou et al., 2005). Simulations of mature WT AZs considered p_r of 0.25 and tight coupling (Schmidt et al., 2013), insensitivity of release to EGTA and Ca_v2.1-SDT. Because the contribution of Ca_v2.3 to synchronous release was negligible, they were omitted here. We found that the properties of mature WT AZs were reproduced if a single, tightly coupled (10 nm) open Ca_v2.1 channel controlled a release site, while Ca_v2.2 channels were located at distances of ≥ 40 nm to release sensors (Figures 4A–4F).

Mutant AZs operated with DOT and less tight coupling. Compared with WT, p_r is halved at *Munc13-3*^{-/-} PF terminals (Ishiyama et al., 2014). Thus, a model of the mutant AZ needed to reproduce p_r of ~0.125, sensitivity of release to EGTA, and DOT of Ca_v2.1 and Ca_v2.2. These requirements were met in the simulations, if two open Ca_v2.1 and one open Ca_v2.2 controlled a release site, with Ca_v2.1 and Ca_v2.2 being located at distances of 24 and 34 nm, respectively, from the release sensor (Figures 4G–4L). Although the contribution of influx through Ca_v2.2 was only 15% of the total Ca²⁺ signal sensed by the release sensors, blocking Ca_v2.2 reduced p_r by ~30%, consistent with the experiments and explained by the non-linear dependency of release on [Ca²⁺]_i (Lou et al., 2005).

DISCUSSION

Mature PF-to-PN synapses operate at nanodomain coupling (Schmidt et al., 2013), which develops from an initial microdomain coupling present at immature AZs (Baur et al., 2015). Here, we extend these findings by showing that *Munc13-3* acts as an important regulator during AZ maturation, determining the subcellular organization of Ca_vs and being required for the correct placement of Ca_v2.1 to establish nanodomain coupling with SDT during development.

Munc13-3 has been shown to increase the p_r of release competent vesicles by “superpriming” (Augustin et al., 2001; Ishiyama et al., 2014), but it remained unclear whether superpriming decreases the coupling distance (positional superpriming) or increases the Ca²⁺ sensitivity of the release machinery (molecular superpriming; Ishiyama et al., 2014). Our present data suggest that *Munc13-3* superprimes vesicles by locating Ca_v2.1 in their nanoscale vicinity, probably at central parts of the AZ (i.e., *Munc13-3*-mediated superpriming is essentially positional).

The sensor model used here was developed at the calyx of Held synapse (Lou et al., 2005), where synaptotagmin-2 (Syt2) is the dominating release sensor (Kochubey and Schneggenburger, 2011). Although it is unclear whether PF_vs express only Syt2 or Syt1 or both (Fox and Sanes, 2007), there is evidence that the

(K) As in (E). Note the supra-linear summation of the toxin sensitive release rates (dashed line) compared with control (solid line).

(L) As in (F). EGTA 4.5 mM (blue) reduced p_r by 28%.

dominating cerebellar release sensor in mice of the age analyzed here is Syt2 (Berton et al., 1997). At present there is no kinetic model for Syt1-triggered fast transmitter release from CNS synapses available, but altering the Ca^{2+} kinetics of Syt2-mediated release within plausible limits had no large impact on estimates of coupling distances (Schmidt et al., 2013). Importantly, the conclusion of Munc13-3 being a developmental regulator of coupling is independent of absolute coupling distance estimates.

Of the four Munc13 isoforms expressed in the brain, only Munc13-1 and Munc13-3 are present in PF_vs (Augustin et al., 2001; Breustedt et al., 2010). Although Munc13-1 is a mandatory priming factor for AP-triggered glutamate release, the remaining Munc13s convey more subtle influences on vesicle fusion, which are isoform and probably also cell-type specific (Südhof, 2012). At PF synapses, Munc13-3 reduces PPR and increases p_r (Augustin et al., 2001; Ishiyama et al., 2014), while at the calyx of Held, PPR was unaffected by loss of Munc13-3, and it had a role in regulating recovery from depression (Chen et al., 2013).

Munc13-3 likely acts in concert with other proteins at the AZ. In immunoprecipitation assays, Munc13-3 co-precipitated with syntaxin, synaptobrevin and SNAP25, which is consistent with an association of Munc13-3 with the exocytotic core complex (Augustin et al., 1999). Via such interaction, Munc13-3 could pull a vesicle closer to the plasma membrane, thereby reducing the physical distance between Syt and Ca_v . However, in light of the fault localization of $\text{Ca}_v2.1$ in mature mutants, it is likely that the major effect results from an additional interaction of Munc13-3 with proteins of the AZ scaffold with known function in vesicle docking and Ca_v recruitment. RIM has been suggested to be the central organizer in this process. Together with RIM-BP it specifically recruits $\text{Ca}_v2.1$ and $\text{Ca}_v2.2$ to the AZ and in concert with Rab3/27 and Munc13-1 tethers vesicles close to these sites (Südhof, 2012). The interaction with Munc13-1 is mediated via its N-terminal C2A domain, which is absent in Munc13-3. However, recently it was shown that the *Drosophila* Unc13A isoform, which also lacks the C2A domain, binds to Bruchpilot (BRP) and RIM-BP via its N terminus (Böhme et al., 2016). Interestingly, Unc13A was further shown to be required for tightening the coupling distance during development of the *Drosophila* neuromuscular junction.

The vertebrate homolog of BRP is ELKS. RIM binds to ELKS, and thus, Munc13-3 could link the core complex to RIM via ELKS and RIM-BP, thereby reducing the distance between Syt and Ca_v . Consistently, ELKS1,2 conditional double-KO as well as BRP mutation result in impaired Ca_v localization and reduced p_r (Kittel et al., 2006; Liu et al., 2014). RIM-BP binds to $\text{Ca}_v2.1$, $\text{Ca}_v2.2$, and $\text{Ca}_v1.2$ (L-type) channels and via interaction with RIM specifically recruits only the former two channels to the AZ. Our results suggest that interaction with Munc13-3 further narrows the spectrum of release driving Ca_v s to $\text{Ca}_v2.1$ with nanodomain coupling to Syt. The N terminus of Munc13-3 may be key in this process.

EXPERIMENTAL PROCEDURES

Experiments were performed on cerebellar slices from P8–P10 and P21–P24 Munc13-3^{-/-}, Munc13-3^{+/+}, and C57Bl6 WT mice of either sex, as described

previously (Baur et al., 2015). Experimental procedures were approved by the state directorate of Saxony, Germany.

Electrophysiology and Ca^{2+} Imaging

EPSCs were recorded at $33 \pm 2^\circ\text{C}$ from whole-cell patch-clamped PNPs and evoked by extracellular PF-tract stimulation. Fluorescence signals were recorded in line scans between 20 and 60 min equilibration time at $22 \pm 1^\circ\text{C}$. Each bouton (typically five to ten per cell) was recorded three times under control conditions and following toxin application. $\Delta\text{G/R}$ from Fluo-5F/Alexa 594 was converted to $[\text{Ca}^{2+}]_i$ on the basis of a cuvette calibration ($R_{\min} = 0.017$, $R_{\max} = 0.835$).

SDS-FRL Immunogold Labeling

Immunogold labeling of replicas was performed on cryoprotected coronal cerebellar sections from brains of two P21 Munc13-3^{+/+} and two Munc13-3^{-/-} mice. VGluT1-positive PF_vs were photographed at a magnification of 8,900 \times .

Modeling

Reaction schemes were converted into corresponding systems of ordinary differential equations (ODEs). Spatial resolution was achieved by placing ODEs into concentric hemi-shells. The sensor model was placed at varying distances from Ca^{2+} sources. Release mediated by distributed Ca^{2+} sources was simulated by driving the sensor by the sum of $[\text{Ca}^{2+}]_i$ from all sources.

Data Presentation and Statistics

Data are presented as box (IQR)-and-whisker plots (farthest points within 1.5-fold IQR [Tukey's definition]); outliers are shown as individual data points. Solid and dashed lines within boxes show medians and means, respectively. Data were compared using t test, rank-sum test, or ANOVA (on ranks), depending on their distribution. Particle distance distributions and clustering were compared using the Kolmogorov-Smirnov test. Statistical significance is denoted as follows: * $p \leq 0.05$, ** $p \leq 0.01$, and *** $p \leq 0.001$.

SUPPLEMENTAL INFORMATION

Supplemental Information includes Supplemental Experimental Procedures, three figures, and one table and can be found with this article online at <https://doi.org/10.1016/j.celrep.2018.02.010>.

ACKNOWLEDGMENTS

We thank Nils Brose for providing Munc13-3 mice, Stefan Hallermann for discussion, and Gudrun Bethge and Natalie Wernet for technical assistance. This work was supported by the German Research Foundation (DFG; grants SCHM1838/1 to H.S. and FOR 2143 to A.K.) and BIOS-2 (to A.K.).

AUTHOR CONTRIBUTIONS

H.S. conceived the study and performed the modeling. V.K., G.B., D.L., J.B., D.B., J.J., and A.K. performed experiments and analyzed the data. H.S., A.K., and G.B. supervised the study. M.W. provided Ca_v antibodies. J.E. and M.H. provided expertise and feedback. G.B., A.K., and H.S. wrote the manuscript.

DECLARATION OF INTERESTS

The authors declare no competing interests.

Received: June 14, 2017

Revised: December 1, 2017

Accepted: January 31, 2018

Published: February 20, 2018

REFERENCES

Adler, E.M., Augustine, G.J., Duffy, S.N., and Charlton, M.P. (1991). Alien intracellular calcium chelators attenuate neurotransmitter release at the squid giant synapse. *J. Neurosci.* **11**, 1496–1507.

- Althof, D., Baehrens, D., Watanabe, M., Suzuki, N., Fakler, B., and Kulik, Á. (2015). Inhibitory and excitatory axon terminals share a common nano-architecture of their $\text{Ca}_v2.1$ (P/Q-type) Ca^{2+} channels. *Front. Cell. Neurosci.* 9, 315.
- Augustin, I., Betz, A., Herrmann, C., Jo, T., and Brose, N. (1999). Differential expression of two novel Munc13 proteins in rat brain. *Biochem. J.* 337, 363–371.
- Augustin, I., Korte, S., Rickmann, M., Kretschmar, H.A., Südhof, T.C., Herms, J.W., and Brose, N. (2001). The cerebellum-specific Munc13 isoform Munc13-3 regulates cerebellar synaptic transmission and motor learning in mice. *J. Neurosci.* 21, 10–17.
- Baur, D., Bornschein, G., Althof, D., Watanabe, M., Kulik, A., Eilers, J., and Schmidt, H. (2015). Developmental tightening of cerebellar cortical synaptic influx-release coupling. *J. Neurosci.* 35, 1858–1871.
- Berton, F., Iborra, C., Boudier, J.A., Seagar, M.J., and Marquèze, B. (1997). Developmental regulation of synaptotagmin I, II, III, and IV mRNAs in the rat CNS. *J. Neurosci.* 17, 1206–1216.
- Böhme, M.A., Beis, C., Reddy-Alla, S., Reynolds, E., Mampell, M.M., Grasskamp, A.T., Lützkendorf, J., Bergeron, D.D., Driller, J.H., Babikir, H., et al. (2016). Active zone scaffolds differentially accumulate Unc13 isoforms to tune Ca^{2+} channel-vesicle coupling. *Nat. Neurosci.* 19, 1311–1320.
- Breustedt, J., Gundlfinger, A., Varoqueaux, F., Reim, K., Brose, N., and Schmitz, D. (2010). Munc13-2 differentially affects hippocampal synaptic transmission and plasticity. *Cereb. Cortex* 20, 1109–1120.
- Bucurenciu, I., Kulik, A., Schwaller, B., Frotscher, M., and Jonas, P. (2008). Nanodomain coupling between Ca^{2+} channels and Ca^{2+} sensors promotes fast and efficient transmitter release at a cortical GABAergic synapse. *Neuron* 57, 536–545.
- Chen, Z., Cooper, B., Kalla, S., Varoqueaux, F., and Young, S.M., Jr. (2013). The Munc13 proteins differentially regulate readily releasable pool dynamics and calcium-dependent recovery at a central synapse. *J. Neurosci.* 33, 8336–8351.
- Delvendahl, I., Jablonski, L., Baade, C., Matveev, V., Neher, E., and Hallermann, S. (2015). Reduced endogenous Ca^{2+} buffering speeds active zone Ca^{2+} signaling. *Proc. Natl. Acad. Sci. U S A* 112, E3075–E3084.
- Eggermann, E., Bucurenciu, I., Goswami, S.P., and Jonas, P. (2011). Nanodomain coupling between Ca^{2+} channels and sensors of exocytosis at fast mammalian synapses. *Nat. Rev. Neurosci.* 13, 7–21.
- Faas, G.C., Schwaller, B., Vergara, J.L., and Mody, I. (2007). Resolving the fast kinetics of cooperative binding: Ca^{2+} buffering by calretinin. *PLoS Biol.* 5, e311.
- Fedchyshyn, M.J., and Wang, L.Y. (2005). Developmental transformation of the release modality at the calyx of Held synapse. *J. Neurosci.* 25, 4131–4140.
- Foster, K.A., Crowley, J.J., and Regehr, W.G. (2005). The influence of multivesicular release and postsynaptic receptor saturation on transmission at granule cell to Purkinje cell synapses. *J. Neurosci.* 25, 11655–11665.
- Fox, M.A., and Sanes, J.R. (2007). Synaptotagmin I and II are present in distinct subsets of central synapses. *J. Comp. Neurol.* 503, 280–296.
- Holderith, N., Lorincz, A., Katona, G., Rózsa, B., Kulik, A., Watanabe, M., and Nusser, Z. (2012). Release probability of hippocampal glutamatergic terminals scales with the size of the active zone. *Nat. Neurosci.* 15, 988–997.
- Indriati, D.W., Kamasawa, N., Matsui, K., Meredith, A.L., Watanabe, M., and Shigemoto, R. (2013). Quantitative localization of $\text{Ca}_v2.1$ (P/Q-type) voltage-dependent calcium channels in Purkinje cells: somatodendritic gradient and distinct somatic co-clustering with calcium-activated potassium channels. *J. Neurosci.* 33, 3668–3678.
- Ishiyama, S., Schmidt, H., Cooper, B.H., Brose, N., and Eilers, J. (2014). Munc13-3 superprimed synaptic vesicles at granule cell-to-basket cell synapses in the mouse cerebellum. *J. Neurosci.* 34, 14687–14696.
- Kittel, R.J., Wichmann, C., Rasse, T.M., Fouquet, W., Schmidt, M., Schmid, A., Wagh, D.A., Pawlu, C., Kellner, R.R., Willig, K.I., et al. (2006). Bruchpilot promotes active zone assembly, Ca^{2+} channel clustering, and vesicle release. *Science* 312, 1051–1054.
- Kochubey, O., and Schneggenburger, R. (2011). Synaptotagmin increases the dynamic range of synapses by driving Ca^{2+} -evoked release and by clamping a near-linear remaining Ca^{2+} sensor. *Neuron* 69, 736–748.
- Li, L., Bischofberger, J., and Jonas, P. (2007). Differential gating and recruitment of P/Q-, N-, and R-type Ca^{2+} channels in hippocampal mossy fiber boutons. *J. Neurosci.* 27, 13420–13429.
- Liu, C., Bickford, L.S., Held, R.G., Nyitrai, H., Südhof, T.C., and Kaeser, P.S. (2014). The active zone protein family ELKS supports Ca^{2+} influx at nerve terminals of inhibitory hippocampal neurons. *J. Neurosci.* 34, 12289–12303.
- Lou, X., Scheuss, V., and Schneggenburger, R. (2005). Allosteric modulation of the presynaptic Ca^{2+} sensor for vesicle fusion. *Nature* 435, 497–501.
- Mintz, I.M., Sabatini, B.L., and Regehr, W.G. (1995). Calcium control of transmitter release at a cerebellar synapse. *Neuron* 15, 675–688.
- Miyazaki, T., Fukaya, M., Shimizu, H., and Watanabe, M. (2003). Subtype switching of vesicular glutamate transporters at parallel fibre-Purkinje cell synapses in developing mouse cerebellum. *Eur. J. Neurosci.* 17, 2563–2572.
- Myoga, M.H., and Regehr, W.G. (2011). Calcium microdomains near R-type calcium channels control the induction of presynaptic long-term potentiation at parallel fiber to purkinje cell synapses. *J. Neurosci.* 31, 5235–5243.
- Sabatini, B.L., Oertner, T.G., and Svoboda, K. (2002). The life cycle of Ca^{2+} ions in dendritic spines. *Neuron* 33, 439–452.
- Schmidt, H., Brachtendorf, S., Arendt, O., Hallermann, S., Ishiyama, S., Bornschein, G., Gall, D., Schiffmann, S.N., Heckmann, M., and Eilers, J. (2013). Nanodomain coupling at an excitatory cortical synapse. *Curr. Biol.* 23, 244–249.
- Scimemi, A., and Diamond, J.S. (2012). The number and organization of Ca^{2+} channels in the active zone shapes neurotransmitter release from Schaffer collateral synapses. *J. Neurosci.* 32, 18157–18176.
- Südhof, T.C. (2012). The presynaptic active zone. *Neuron* 75, 11–25.
- Vyleta, N.P., and Jonas, P. (2014). Loose coupling between Ca^{2+} channels and release sensors at a plastic hippocampal synapse. *Science* 343, 665–670.
- Yang, Y.M., Fedchyshyn, M.J., Grande, G., Aitoubah, J., Tsang, C.W., Xie, H., Ackerley, C.A., Trimble, W.S., and Wang, L.Y. (2010). Septins regulate developmental switching from microdomain to nanodomain coupling of Ca^{2+} influx to neurotransmitter release at a central synapse. *Neuron* 67, 100–115.